Quantum cascade of correlated phases in trigonally warped bilayer graphene

https://doi.org/10.1038/s41586-022-04937-1

Received: 6 November 2021

Accepted: 7 June 2022

Published online: 10 August 2022

Check for updates

Anna M. Seiler[1,2], Fabian R. Geisenhof[2], Felix Winterer[2], Kenji Watanabe[3], Takashi Taniguchi[4], Tianyi Xu[5], Fan Zhang[5]✉ & R. Thomas Weitz[1,2,6]✉

Divergent density of states offers an opportunity to explore a wide variety of correlated electron physics. In the thinnest limit, this has been predicted and verified in the ultraflat bands of magic-angle twisted bilayer graphene[1–5], the band touching points of few-layer rhombohedral graphite[6–8] and the lightly doped rhombohedral trilayer graphene[9–11]. The simpler and seemingly better understood Bernal bilayer graphene is also susceptible to orbital magnetism at charge neutrality[7] leading to layer antiferromagnetic states[12] or quantum anomalous Hall states[13]. Here we report the observation of a cascade of correlated phases in the vicinity of electric-field-controlled Lifshitz transitions[14,15] and van Hove singularities[16] in Bernal bilayer graphene. We provide evidence for the observation of Stoner ferromagnets in the form of half and quarter metals[10,11]. Furthermore, we identify signatures consistent with a topologically non-trivial Wigner–Hall crystal[17] at zero magnetic field and its transition to a trivial Wigner crystal, as well as two correlated metals whose behaviour deviates from that of standard Fermi liquids. Our results in this reproducible, tunable, simple system open up new horizons for studying strongly correlated electrons.

Electron–electron interactions can give rise to macroscopic quantum phenomena such as magnetism, superconductivity and quantum Hall (QH) effects. It is well known that interaction effects can be boosted near where the density of states (DOS) of electrons diverges. One remarkable example is twisted bilayer graphene, in which the Dirac minibands become flattest when the twist angle is near the so-called magic angle[1]. Indeed, orbital ferromagnetism[18], the quantum anomalous Hall (QAH) effect[19] and nematic superconductivity[20] have been observed in this delicately designed system[5]. In fact, strongly interacting behaviour has also been discovered in the simpler, naturally occurring, Bernal bilayer graphene (BLG) at charge neutrality. Under a high magnetic field, its bands quantize into Landau levels (LL) that are exactly flat, and both the fractional QH effect and QH ferromagnetism have been reported[6,13,21,22]. Near zero magnetic field, its quadratic band touching points that each has a non-trivial winding number of ±2 are susceptible to spontaneous gaps driven by topological orbital magnetism[7], as evidenced by a QAH octet observed in free-standing BLG[13]. Interestingly, when lightly doped, the trigonal warping of the Fermi surface of BLG (and its rhombohedral cousins) attributed to the interlayer next-nearest-neighbour coupling[23] becomes pronounced. The winding number and the C_{3z} symmetry dictate a deformation of each quadratic cone into one central Dirac cone and three surrounding ones. An electric field can gap these cones and even invert the central one[14,15]. These produce multiple Lifshitz transitions and van Hove singularities (vHSs) tunable by the electric field and the charge density. However, so far, correlated phases mediated by this trigonal warping effect have escaped experimental observation in BLG, although ferromagnetism and superconductivity have been recently reported in lightly doped rhombohedral trilayer graphene (RTG)[10,11].

Here we show that, at large electric fields, gate-tunable correlated insulating and metallic phases emerge in lightly doped high-quality BLG, without the presence of a moiré potential. The two insulating phases are consistent with a Wigner crystal and an unprecedented Wigner–Hall crystal, respectively, and the novel metallic phases are most likely fractional metals that develop LLs and correlated metals that show no signs of Landau quantization.

The investigated BLG flakes are encapsulated in hexagonal boron nitride (hBN) and equipped with graphite top and bottom gates as well as graphite contacts in a two-terminal configuration (Extended Data Fig. 1 and Methods). By varying both gate voltages, the charge carrier density n and the perpendicular electric field E can be tuned. Figure 1a shows the two-terminal conductance G in arbitrary units (a.u.) measured at zero magnetic field B and a temperature T of 10 mK. A crystallographic alignment between the BLG, hBN and graphite contacts that would produce a moiré pattern can be excluded, given the clear absence of additional conductance minima at higher density[24,25].

Magnetotransport in bilayer graphene

We focus our discussions on the hole side at large electric fields where the most distinctive features are observed; an onset of similar physics is observed on the electron side, and the features at low electric fields[6,14,15,24,25] exemplify the ultrahigh quality of our devices (Methods and Extended Data Figs. 2 and 3). At larger electric fields, the trigonal warping becomes more visible as the central hole pocket is inverted into an electron pocket at lower energies (Fig. 1b,f). At very low doping, the Fermi surface is consequently composed of three disconnected

[1]1st Physical Institute, Faculty of Physics, University of Göttingen, Göttingen, Germany. [2]Physics of Nanosystems, Department of Physics, Ludwig-Maximilians-Universität München, Munich, Germany. [3]Research Center for Functional Materials, National Institute for Materials Science, Tsukuba, Japan. [4]International Center for Materials Nanoarchitectonics, National Institute for Materials Science, Tsukuba, Japan. [5]Department of Physics, University of Texas at Dallas, Richardson, TX, USA. [6]Center for Nanoscience (CeNS), Munich, Germany. ✉e-mail: zhang@utdallas.edu; thomas.weitz@uni-goettingen.de

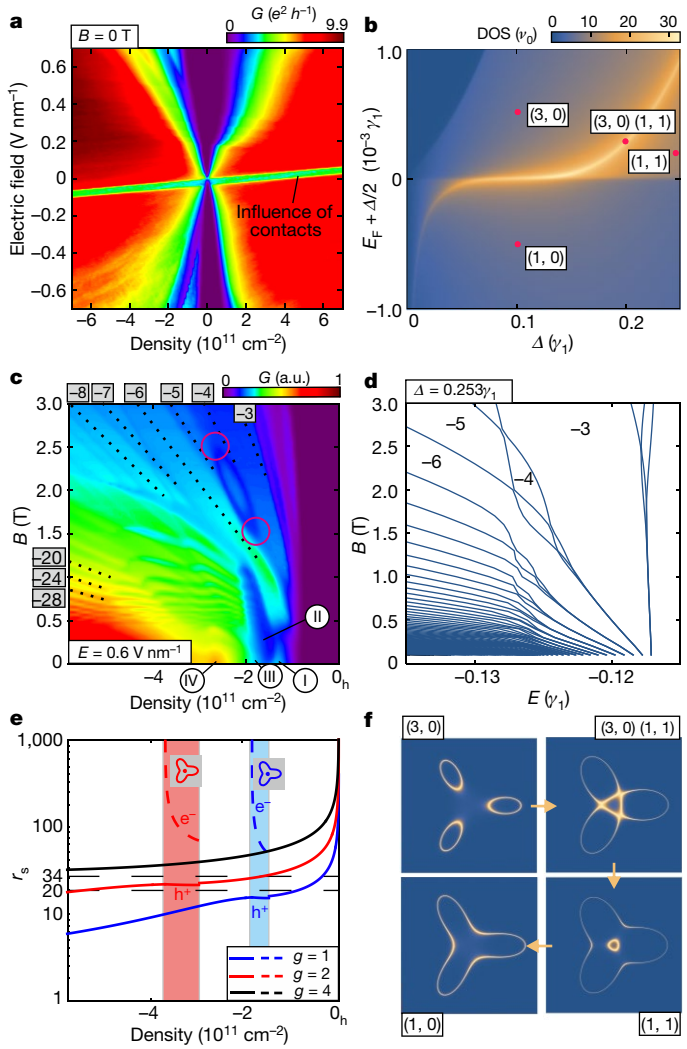

Fig. 1 | Magnetotransport in bilayer graphene. a, Conductance map as a function of E and n measured at $B = 0$ T and $T = 10$ mK. **b**, Calculated DOS as a function of the interlayer potential difference Δ and the Fermi energy E_F (in units of the constant DOS ν_0 of the BLG without trigonal warping). The red dots correspond to the calculated Fermi surfaces shown in **f**. The Fermi surface topology is classified by two invariants (i,j), where i and j are the numbers of hole and electron pockets, respectively. The brightest line manifests the vHS at the Lifshitz transition between the (3, 0) and the (1, 0) Fermi surfaces for $\Delta < 0.1\gamma_1$ or the (3, 0) and the (1, 1) Fermi surfaces for $\Delta > 0.1\gamma_1$. The $E_F = -\Delta/2$ line at $\Delta > 0.1\gamma_1$ shows the (dis)appearance of the central electron pocket at the Lifshitz transition between the (1, 1) and the (1, 0) Fermi surfaces. **c**, Fan diagram of the conductance at $E = 0.6$ V nm^{-1}. QH states are traced by black dotted lines and corresponding filling factors (ν) are indicated by arabic numerals. The two crossings between the $\nu = -4$ and $\nu = -5$ QH states are highlighted by red circles. New correlated phases are indicated by roman numerals. **d**, Calculated LL spectrum at $\Delta = 0.253\gamma_1$ for a non-degenerate Fermi surface. Δ is the interlayer potential difference induced by E. $\gamma_1 \approx 400$ meV is the interlayer nearest-neighbour coupling. The filling factors of QH states are indicated by arabic numerals. **e**, The calculated Wigner–Seitz radius r_s as a function of n (see Methods for details) for the quadruply ($g = 4$, black line), doubly ($g = 2$, red lines) and singly ($g = 1$, blue lines) degenerate Fermi surfaces, respectively. The solid lines are for the outer hole (h^+) pockets and the dashed lines are for the inner electron (e^-) pockets. The shaded regions are where the Fermi surface is annular between the two Lifshitz transitions. $r_s = 20$ and $r_s = 34$ are the thresholds for the ferromagnetic instability and the Wigner crystallization of 2D electron gases, respectively. **f**, Calculated trigonally warped Fermi surfaces under a large E field. The classifying invariants (i,j) are defined in **b** above. The arrows indicate the two Lifshitz transitions with increasing $|n|$.

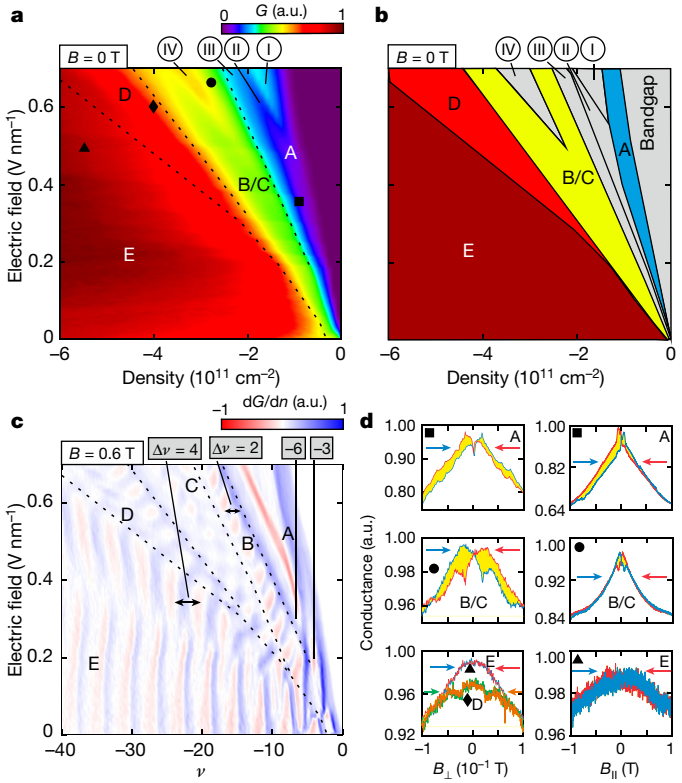

Fig. 2 | Stoner ferromagnetism in bilayer graphene. a, Conductance map as a function of E and n measured at $B = 0$ T for the valence band and positive electric fields. Stoner phases are labelled with the letters A–E and separated by dashed lines. New correlated phases are labelled by the roman numerals I–IV. **b**, Schematic of the phase diagram shown in **a**. **c**, Density derivative of conductance as a function of E and ν at $B = 0.6$ T. **d**, Hysteresis of the conductance as a function of the out-of-plane and in-plane magnetic fields in phase A ($n = -8.5 \times 10^{10}$ cm^{-2}, $E = 0.36$ V nm^{-1}), phase B/C ($n = -2.6 \times 10^{11}$ cm^{-2}, $E = 0.65$ V nm^{-1}), phase D ($n = -4.0 \times 10^{11}$ cm^{-2}, $E = 0.6$ V nm^{-1}) and phase E ($n = -5.5 \times 10^{11}$ cm^{-2}, $E = 0.5$ V nm^{-1}). The forward sweeps in **d** are shown in blue (green for phase D) and the backwards ones in red (orange for phase D). The hysteresis loop areas are shaded in yellow.

hole pockets ((3, 0) panel in Fig. 1f) that move apart with increasing E. At slightly higher doping, these three pockets connect, and the Fermi surface undergoes the first Lifshitz transition featuring a vHS and then becomes an annulus, that is, an inner electron pocket and an outer hole pocket ((1, 1) panel in Fig. 1f). As the doping increases further, the hole pocket enlarges whereas the electron pocket contracts and disappears in the second Lifshitz transition ((1, 0) panel in Fig. 1f). Figure 1c shows the Landau fan diagram at $E = 0.6$ V nm^{-1}. At very low doping, the three disconnected hole pockets result in a three-fold LL degeneracy per spin–valley, and only the filling factor $\nu = -3$ and $\nu = -6$ QH ferromagnetic states emerge at $B < 1.2$ T (Fig. 1c and Extended Data Fig. 3g), whereas at $B > 2.5$ T all the integer QH ferromagnetic states are resolved. Between 1.5 T and 2.5 T there are two crossings between the $\nu = -4$ and $\nu = -5$ QH states, originating from the emergence and contraction of the inner electron pocket (Fig. 1f) whose LLs do not mix with the hole LLs[14,15]. The magnetic fields and densities associated with the observed LL crossings match well with the calculated LL spectrum (Fig. 1d) and density range with an annular Fermi surface (Fig. 1e) for the non-degenerate case.

Moreover, at $B < 1.3$ T, the conductance pattern strongly deviates from any conventional LL sequence (Fig. 1c). For example, in sharp contrast to the established single-particle picture[6,26], a complex non-monotonous E- and n-dependent variation of the conductance emerges for $E > 0.1$ V nm^{-1} even at $B = 0$ (Fig. 1a). Below we identify

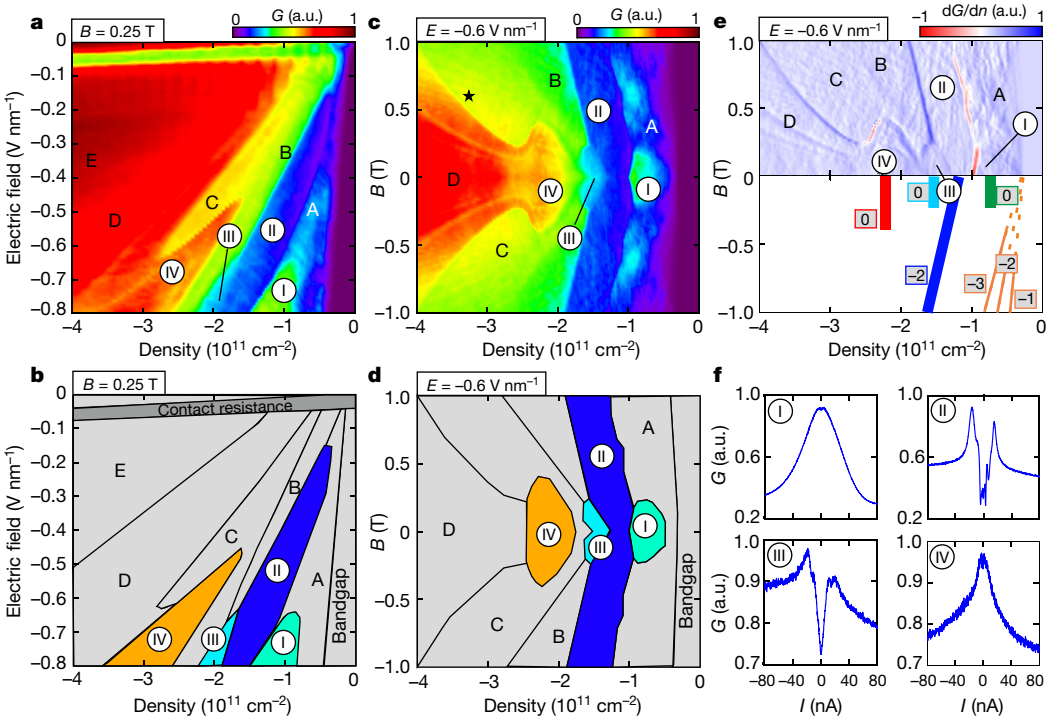

Fig. 3 | New correlated phases at large electric fields. a, Conductance map as a function of E and n measured at $B = 0.25$ T for the valence band and negative electric fields. Stoner phases are labelled with the letters A–E. New correlated phases are labelled by the roman numerals I–IV. **b**, Schematic of the phase diagram shown in **a**. **c**, Conductance map as a function of B and n measured at $E = -0.6$ V nm^{-1}. Indication of the onset of insulating phase V is marked by a star (Extended Data Fig. 12). **d**, Schematic of the phase diagram shown in **c**. **e**, Top: density derivative of the conductance in **c**. Bottom: schematic of the slopes of the lowest integer QH states and the phases I–IV. The corresponding slopes are indicated by arabic numerals. The lines are solid if the states are present and dashed otherwise. **f**, Conductance as a function of d.c. current bias for the phases I–IV at $E = -0.6$ V nm^{-1} and $B = 0$ T. The corresponding densities are $n = 0.8 \times 10^{11}$ cm^{-2} for phase I, $n = 1.1 \times 10^{11}$ cm^{-2} for phase II, $n = 1.4 \times 10^{11}$ cm^{-2} for phase III and $n = 2.2 \times 10^{11}$ cm^{-2} for phase IV.

various phases (A–E and I–V) by their conductance and evolution in the space of temperature, density, magnetic and electric fields, and bias current. This unexpected phase diagram of BLG stems from the intricate interplay between electron–electron interaction and trigonal warping.

Stoner spin–valley ferromagnetism

The prominent steps in the conductance that already start to appear at low electric fields above 0.1 V nm^{-1} in Fig. 1a are highlighted in Fig. 2a,b for positive electric fields. We label regions of different constant conductance with the letters A–E. Their E and n dependence is reminiscent of those of half and quarter metals with spontaneous spin–valley polarization or coherence observed recently in RTG[10], analogous to the textbook Stoner ferromagnets. Indeed, the experimental signatures observed in our BLG agree well with the exchange-interaction-driven ferromagnetic phases that can be well resolved at $B = 0.6$ T (Fig. 2c).

Phase A is close to the valence-band edge, and the $\nu = -3$ and $\nu = -6$ QH states emerge owing to the three-fold degeneracy of the trigonally warped Fermi surface ((3, 0) panel in Fig. 1f). This phase shows slight out-of-plane magnetic hysteresis but a large in-plane one (Fig. 2d), and is most consistent with a quarter metal with in-plane spin polarization and inter-valley coherence. At higher densities, phase B/C emerges at $B = 0$. At finite magnetic fields, this phase splits up into two distinct phases B and C. Phase B exhibits two-fold LL degeneracy consistent with a half metal[10] (Fig. 2c). Its strong hysteresis that is of the same order in in-plane and out-of-plane magnetic fields (Fig. 2d) is indicative of spin polarization. Unlike phases A and B, phase C exhibits conductance oscillations versus E instead of n, possibly owing to a partial polarization or a more complex order. Phase D shows similar LL degeneracy and conductance oscillations to phase C (Fig. 2c) but no magnetic hysteresis (Fig. 2d), which may indicate inter-valley coherence. Phase E emerges at higher densities, exhibits four-fold LL degeneracy (Fig. 2c) and an absence of magnetic hysteresis (Fig. 2d), and is most consistent with a full metal without spin–valley polarization.

Consistently, our calculation for $E = 0.6$ V nm^{-1} and the measured densities reveals that with four-fold or two-fold degeneracy, the Wigner–Seitz radius r_s exceeds 20 (Fig. 1e and Methods), a threshold for the ferromagnetic instability of two-dimensional (2D) electron gases[27]. Moreover, phases A, B and E are below the first Lifshitz transitions and the vHS of the non-, two-fold- and four-fold-degenerate Fermi surfaces, respectively, whereas phases C and D are on the two sides of the second Lifshitz transition of the doubly degenerate Fermi surface (Figs. 1e and 2c). As the DOS of BLG is smaller than that of RTG, phases A–E emerge in narrower density ranges.

New correlated metallic and insulating phases

Besides the Stoner phases, we can also identify several phases that compete with them yet have not been previously reported in graphene systems. We focus hereafter on these new phases in the large-negative-electric-field range, and there are at least four distinct phases at $B = 0$ (I–IV, Fig. 3a–d) that can be identified by steps in the conductance and stabilities in the space of T, n, B, E and bias current I. All four phases were also identified in a second device (Methods and Extended Data Fig. 4). For low doping, the conductance increases with increasing density until it reaches a plateau (phase I). The conductance then drops significantly (phase II) with further increasing density until it increases again (phase III). In addition, another plateau of higher conductance can be observed at still higher densities (phase IV). Although these phases are all unstable against the Stoner phases at large magnetic fields ($B > 0.5$–1.5 T), their mutual phase boundaries

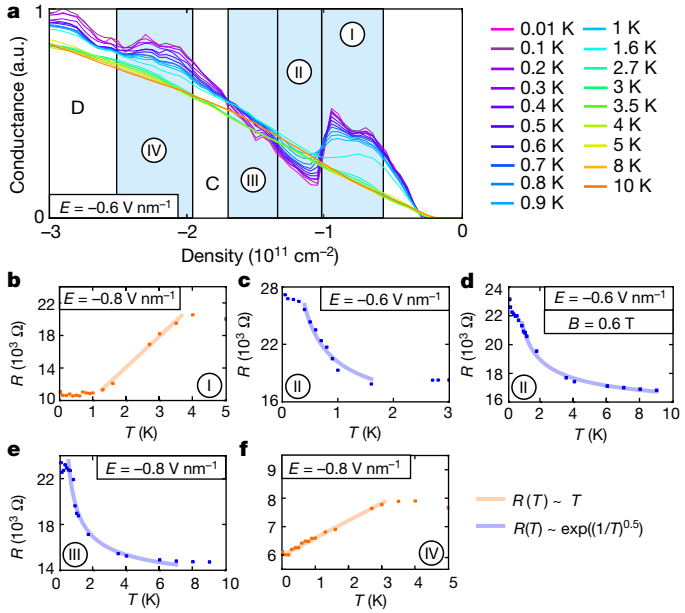

Fig. 4 | Temperature stability of new correlated phases. a, Conductance as a function of n at $E = -0.6$ V nm^{-1} and different temperatures. The new correlated phases I–IV are highlighted in light blue. **b**–**f**, Temperature dependence of the resistance in phase I at $n = -1.3 \times 10^{11}$ cm^{-2}, $E = -0.8$ V nm^{-1} and $B = 0$ T (**b**), phase II at $n = -1.2 \times 10^{11}$ cm^{-2}, $E = -0.6$ V nm^{-1} and $B = 0$ T (**c**), phase II at $n = -1.4 \times 10^{11}$ cm^{-2}, $E = -0.6$ V nm^{-1} and $B = 0.6$ T (**d**), phase III at $n = -2.0 \times 10^{11}$ cm^{-2}, $E = -0.8$ V nm^{-1} and $B = 0$ T (**e**), and phase IV at $n = -3.2 \times 10^{11}$ cm^{-2}, $E = -0.8$ V nm^{-1} and $B = 0$ T (**f**). The linear temperature dependence in phases I and IV is highlighted by orange lines. For phases II and III $R(T) = R_0 e^{\sqrt{T_0/T}}$ (blue lines) is fitted by using $R_0 = 12{,}932.36\ \Omega$ and $T_0 = 0.1978$ K in **c**, $R_0 = 13{,}581.63\ \Omega$ and $T_0 = 0.1199$ K in **d**, and $R_0 = 12{,}142.09\ \Omega$ and $T_0 = 0.2189$ K in **e**.

and those with the Stoner phases exhibit sharp conductance changes at small magnetic fields (Fig. 3a–e).

Phase I is an island of relatively high conductance at very low densities close to the valence-band edge. It occurs in the density range below the first Lifshitz transition with a concomitant vHS of the non-degenerate Fermi surface (Fig. 1e) and exhibits an E-dependent phase boundary in the space of n and B against phase A (Fig. 3c–e and Extended Data Figs. 5 and 6). Its intimate connection to the trigonal warping and the layer polarization is also evidenced by the observation that its centre and extent in density increase with increasing electric field (Fig. 3a,b and Extended Data Fig. 6). Phase I exhibits intrinsic magnetism, as revealed by its magnetic hysteresis (Extended Data Figs. 5 and 7) that is, however, smaller than that of phase A. The in-plane magnetic hysteresis is larger than the out-of-plane one, indicating its in-plane spin order and inter-valley coherence. Moreover, large out-of-plane magnetic fields (Fig. 3c–e and Extended Data Fig. 8a) or applied bias currents (Fig. 3f and Extended Data Fig. 9) suppress phase I, which suggests that it is a correlated metal. This is further confirmed by the strong linear temperature dependence $dR/dT = 5{,}000\ \Omega\ K^{-1}$ with resistance $R = 1/G$ in phase I, compared with the 'normal' metallic phase at $E = 0$ and the Stoner phases (Fig. 4d and Extended Data Fig. 10); this linear behaviour is similar to that of strange metals observed in twisted bilayer graphene[28]. Surprisingly, although at low electric fields LLs are visible down to 0.2 T (Extended Data Fig. 3b), phase I shows no signs of Landau quantization, which could result from the possible large effective masses, open Fermi surfaces or strange-metal properties of this phase that require future inspection.

At slightly higher densities, an abrupt transition from phase I to phase II of lower conductance is visible (Fig. 3a–d and Extended Data Fig. 5). Remarkably, phase II shows an increasing resistance with decreasing temperature (Fig. 4c,d), which is indicative of an energy gap, and its low-temperature conductance not only matches that of the $\nu = -2$ QH state but also features a slope of −2 in the fan diagram (Fig. 3c–e and Extended Data Fig. 3g). The presence of an energy gap is also supported by a sudden increase in conductance at large increasing bias currents (Fig. 3f). These together provide strong evidence for a QAH phase with a Chern number of −2. In sharp contrast to the QAH octet reported in free-standing BLG[13], this QAH phase II is stabilized at finite densities that increase with increasing electric field (Fig. 3a,b and Extended Data Fig. 8e), which implies an intimate connection to the trigonal warping. Indeed, our calculation shows that phase II emerges between the two Lifshitz transitions of the non-degenerate annular Fermi surface (Fig. 1e) in which $r_s > 34$, a threshold for the Wigner crystallization of 2D electron gases[27], for the electron pocket. It can be suppressed by the magnetic field (Extended Data Fig. 8b), bias currents (Fig. 3f) and temperature (Fig. 4), but this QAH phase II is present at $B = 0$ T for 0.3 V nm^{-1} < E < 0.8 V nm^{-1} (Extended Data Fig. 6). While for $E < 0.6$ V nm^{-1} a larger electric field stabilizes it against the magnetic field, for $E > 0.8$ V nm^{-1} phase II becomes less stable to the magnetic field (Extended Data Figs. 6 and 8b).

The observation of a QAH phase emerging at $B = 0$ yet $n \neq 0$ is extraordinary. This indicates a topological gap opening at densities where the non-interacting phase and even the Stoner phases would not be gapped. Given that phase II with a large r_s in theory is topologically insulating, compressible in extremely low density and incommensurate with the BLG lattice, most consistent is a Wigner–Hall crystal phase, that is, an electron crystal with a quantized Hall conductance. Indeed, the temperature-dependent resistance scales as $R(T) \sim e^{\sqrt{T_0/T}}$ with a scaling parameter T_0, consistent with the anticipated Efros–Shklovskii hopping transport for electron crystals[29] (Fig. 4c,d). Such a Wigner–Hall crystal at a finite magnetic field was originally proposed by ref. [17], and here phase II may be viewed as its anomalous counterpart at $B = 0$. Elegantly, Wigner–Hall crystals can be described by the Diophantine equation (Methods).

Phase II is unstable to another gapped phase III at slightly higher densities. The two phases compete in nearly the same density space (Fig. 3a–e), and phase III dominates for $E > 0.8$ V nm^{-1} at $B = 0$ (Extended Data Fig. 6). Phase III shows a similar resistance and temperature scaling to phase II (Fig. 4e) but shows neither a slope nor a sign of any LL in the fan diagram, and in fact it can be suppressed by the magnetic field (Fig. 3c–e). Along a similar line of arguments, a potential candidate for phase III is a Wigner crystal. Phases II and III exhibit magnetic hysteresis of similar magnitudes, with stronger in-plane ones (Extended Data Fig. 7). Their phase boundary does not shift with increasing in-plane magnetic field (Extended Data Fig. 11). This suggests that phases II and III probably carry similar in-plane spin order and inter-valley coherence. Compared with phase I, both phases probably have larger magnitudes of spin polarization as they are more stable against large in-plane magnetic fields.

At higher densities the system enters a metallic phase IV of high conductance but unstable at the magnetic fields that favour the Stoner phases. In the fan diagram (Fig. 3c–e), phase IV has a similar shape to phase I but a larger critical magnetic field that increases with increasing E (Extended Data Fig. 8d). Phase IV competes with the half metals B/C and appears close to but below the vHS of the doubly degenerate Fermi surface (Fig. 1e). Compared with phase I, phase IV shows stronger and more isotropic magnetic hysteresis (Extended Data Fig. 7). Its linear temperature-dependent resistance (Fig. 4f) and stability in density, electric and magnetic fields, and bias current (Fig. 3f) are very similar to phase I. These together suggest phase IV to be a spin polarized correlated metal.

Discussion and outlook

Our results reveal a cascade of density- and field-dependent correlated phases in BLG. Transport evidence is provided for Stoner phases including the half and quarter metals, electron crystals including the Wigner

crystal and the unprecedented Wigner–Hall crystal (topologically non-trivial), and two correlated metals whose behaviour deviates from that of standard Fermi liquids. Indicated by the tunable vHS and the large r_s (Fig. 1e), these new phases are driven by the complex interplay between electron–electron interaction, Fermi surface trigonal warping with vHS and the interlayer electric field. However, deciphering the origin of each phase and deeper understanding of this strongly correlated electron system call for further experiments and more theoretical works. Likely there exist finer and weaker phases such as the Stoner phase E and another gapped phase V (Methods and Extended Data Fig. 12).

Note added in proof: During the submission of our work, we became aware of two related experimental works by Zhou et al.[30] and de la Barrena et al.[31] on trigonally warped Bernal bilayer graphene. They both reported the metallic Stoner phases but not the new correlated phases (I–V) with metallic and insulating behaviour.

Online content

Any methods, additional references, Nature Research reporting summaries, source data, extended data, supplementary information, acknowledgements, peer review information; details of author contributions and competing interests; and statements of data and code availability are available at https://doi.org/10.1038/s41586-022-04937-1.

1. Bistritzer, R. & MacDonald, A. H. Moiré bands in twisted double-layer graphene. *Proc. Natl Acad. Sci. USA* **108**, 12233–12237 (2011).
2. Cao, Y. et al. Correlated insulator behaviour at half-filling in magic-angle graphene superlattices. *Nature* **556**, 80–84 (2018).
3. Cao, Y. et al. Unconventional superconductivity in magic-angle graphene superlattices. *Nature* **556**, 43–50 (2018).
4. Shen, C. et al. Correlated states in twisted double bilayer graphene. *Nat. Phys.* **16**, 520–525 (2020).
5. Lau, C. N., Bockrath, M. W., Mak, K. F. & Zhang, F. Reproducibility in the fabrication and physics of moiré materials. *Nature* **602**, 41–50 (2022).
6. Weitz, R. T., Allen, M. T., Feldman, B. E., Martin, J. & Yacoby, A. Broken-symmetry states in doubly gated suspended bilayer graphene. *Science* **330**, 812–816 (2010).
7. Zhang, F., Jung, J., Fiete, G. A., Niu, Q. & MacDonald, A. H. Spontaneous quantum Hall states in chirally stacked few-layer graphene systems. *Phys. Rev. Lett.* **106**, 156801 (2011).
8. Shi, Y. et al. Electronic phase separation in multilayer rhombohedral graphite. *Nature* **584**, 210–214 (2020).
9. Zhang, F., Sahu, B., Min, H. & MacDonald, A. H. Band structure of ABC-stacked graphene trilayers. *Phys. Rev. B* **82**, 35409 (2010).
10. Zhou, H. et al. Half and quarter metals in rhombohedral trilayer graphene. *Nature* **598**, 429–433 (2021).
11. Zhou, H., Xie, T., Taniguchi, T., Watanabe, K. & Young, A. F. Superconductivity in rhombohedral trilayer graphene. *Nature* **598**, 434–438 (2021).
12. Velasco, J. et al. Transport spectroscopy of symmetry-broken insulating states in bilayer graphene. *Nat. Nanotechnol.* **7**, 156–160 (2012).
13. Geisenhof, F. R. et al. Quantum anomalous Hall octet driven by orbital magnetism in bilayer graphene. *Nature* **598**, 53–58 (2021).
14. Varlet, A. et al. Anomalous sequence of quantum Hall liquids revealing a tunable Lifshitz transition in bilayer graphene. *Phys. Rev. Lett.* **113**, 116602 (2014).
15. Varlet, A. et al. Tunable Fermi surface topology and Lifshitz transition in bilayer graphene. *Synth. Met.* **210**, 19–31 (2015).
16. Shtyk, A., Goldstein, G. & Chamon, C. Electrons at the monkey saddle: a multicritical Lifshitz point. *Phys. Rev. B* **95**, 35137 (2017).
17. Tešanović, Z., Axel, F. & Halperin, B. I. "Hall crystal" versus Wigner crystal. *Phys. Rev. B* **39**, 8525–8551 (1989).
18. Sharpe Aaron, L. et al. Emergent ferromagnetism near three-quarters filling in twisted bilayer graphene. *Science* **365**, 605–608 (2019).
19. Serlin, M. et al. Intrinsic quantized anomalous Hall effect in a moiré heterostructure. *Science* **367**, 900–903 (2020).
20. Cao Yuan, et al. Nematicity and competing orders in superconducting magic-angle graphene. *Science* **372**, 264–271 (2021).
21. Kou, A. et al. Electron–hole asymmetric integer and fractional quantum Hall effect in bilayer graphene. *Science* **345**, 55–57 (2014).
22. Ki, D.-K., Fal'ko, V. I., Abanin, D. A. & Morpurgo, A. F. Observation of even denominator fractional quantum Hall effect in suspended bilayer graphene. *Nano Lett.* **14**, 2135–2139 (2014).
23. McCann, E. & Fal'ko, V. I. Landau-level degeneracy and quantum Hall effect in a graphite bilayer. *Phys. Rev. Lett.* **96**, 86805 (2006).
24. Yankowitz, M. et al. Emergence of superlattice Dirac points in graphene on hexagonal boron nitride. *Nat. Phys.* **8**, 382–386 (2012).
25. Dean, C. R. et al. Hofstadter's butterfly and the fractal quantum Hall effect in moiré superlattices. *Nature* **497**, 598–602 (2013).
26. Zhang, Y. et al. Direct observation of a widely tunable bandgap in bilayer graphene. *Nature* **459**, 820–823 (2009).
27. Giuliani, G. & Vignale, G. *Quantum Theory of the Electron Liquid* (Cambridge Univ. Press, 2005).
28. Jaoui, A. et al. Quantum critical behaviour in magic-angle twisted bilayer graphene. *Nat. Phys.* **18**, 633–638 (2022).
29. Abrahams, E., Kravchenko, S. V. & Sarachik, M. P. Metallic behavior and related phenomena in two dimensions. *Rev. Mod. Phys.* **73**, 251–266 (2001).
30. Zhou, H. et al. Isospin magnetism and spin-polarized superconductivity in Bernal bilayer graphene. *Science* **375**, 774–778 (2022).
31. de la Barrera, S. C. et al. Cascade of isospin phase transitions in Bernal-stacked bilayer graphene at zero magnetic field. *Nat. Phys.* https://doi.org/10.1038/s41567-022-01616-w (2022).

Methods

Device fabrication

Bilayer graphene flakes, graphite flakes and hBN flakes, synthesized as described previously[32], were exfoliated on silicon (Si)/silicon dioxide (SiO_2) substrates and subsequently identified with optical microscopy. Raman spectroscopy was used to confirm the number of layers of the bilayer graphene flakes. The encapsulated bilayer graphene devices were fabricated using the same dry transfer method as described in ref. [33]. An hBN flake, two few-layer graphite flakes serving as contacts, a bilayer graphene flake, a lower hBN flake and a graphite flake serving as a bottom gate were picked up and then placed onto a highly doped Si/SiO_2 substrate. Afterwards, the samples were annealed in a vacuum chamber at 200 °C for 12 h. In a second step, a top hBN flake and, subsequently, a graphite flake serving as a top gate were picked up and released onto the annealed heterostructures. The thicknesses of the hBN flakes serving as dielectrics were determined to be 34 nm (top dielectric of device A), 42 nm (bottom dielectric of device A), 13 nm (top dielectric of device B) and 32 nm (bottom dielectric of device B) by using atomic force microscopy. Metal contacts (chromium/gold, 5 nm/60 nm for device A and 2 nm/45 nm for device B) that connect the graphite contacts and gates with larger pads were then structured using electron-beam lithography and were evaporated onto the sample. Optical images and a schematic of our devices are shown in the Extended Data Fig. 1.

Electrical measurements

All quantum transport measurements were conducted in a dilution refrigerator equipped with a superconducting magnet. Unless stated otherwise, the sample temperature was 10–20 mK. Two-terminal conductance measurements were performed using an a.c. bias current of 1–10 nA at 78 Hz using Stanford Research Systems SR865A and SR830 lock-in amplifiers. Home-built low-pass filters were used to reduce high-frequency noises. Gate voltages were applied using Keithley 2450 SourceMeters.

Device characterization

The charge carrier density (n) and the electric field (E) can be tuned independently by varying the top-gate and bottom-gate voltages (V_t and V_b, respectively) and are defined as follows:

$$n = \frac{1}{e}(C_t V_t + C_b V_b)$$

and

$$E = \frac{1}{2\varepsilon_0}(C_t V_t - C_b V_b)\ ,$$

where ε_0 is the vacuum permittivity, and C_t and C_b are the top-gate and bottom-gate capacitances. C_t and C_b were extracted at low electric fields by aligning the integer QH plateaus at finite magnetic fields with their corresponding slopes in a fan diagram (Extended Data Fig. 3a,b). The observed LL crossings at different filling factors (Extended Data Fig. 3c,d) show excellent agreement with those observed previously[6,34,35]. Owing to the screening of Coulomb interaction by hBN, the interaction induced spontaneously gapped phase at $E = 0$ and $n = 0$ is absent, unlike in free-standing BLG[6,12,13,36].

Comment on graphite contacts

Using graphite contacts allows us to avoid etching into the insulating hBN layers, which is usually required for metal contacting but would lower the accessible electric-field range. However, using graphite contacts makes it technically demanding to use four-probe contacts, and thus two-point measurements were used here.

At $B = 0$, we see a line of decreased conductance across $E = 0$ that depends only on the applied bottom-gate voltage but is independent of the top-gate voltage (Extended Data Fig. 3f). We assume that this effect comes from the region of the BLG that is located below the graphite contacts. Here the contacts screen the field of the top gate, which is why we observe only a dependence of the bottom gate. It is worth noting that all the correlated phases that we observe depend on both the top gate and the bottom gate (Extended Data Fig. 3f) and can therefore not be related to the line of decreased conductance that depends on only the bottom-gate voltage. Apart from this line, we see no sudden changes in conductance as a function of density and electric field at small electric fields where the physics is known (Extended Data Fig. 3).

The contact resistance is also visible in the presence of a magnetic field. By tracing the measured conductance along one QH state as a function of the magnetic field, one can observe a linearly decreasing conductance with increasing magnetic field (without any steps in the conductance, right panel in Extended Data Fig. 3a), which we attribute to a magnetic-field-dependent contact resistance of our graphite contacts. This makes it difficult to extract contact resistances for entire fan diagrams. Thus, the measured conduction is given in arbitrary units in most of the figures. Nevertheless, the contact resistance can be determined and subtracted for constant magnetic fields by recording density versus conductance sweeps and by assigning the resistance plateaus to the assigned fillings factors. An exemplary density versus conductance sweep is shown for $B = 2$ T and $E = 0.08$ V nm^{-1} in Extended Data Fig. 3e. Here, the contact resistance was determined to be 7,800 Ω.

At large electric fields, we can also subtract a linearly magnetic-field-dependent contact resistance and find constant conductances in filling factors, and can further determine the conductance of phase II to be approximately $2\,e^2\,h^{-1}$, where e is the charge of a bare electron, and h is Planck's constant (Extended Data Fig. 3g). Owing to the dependence of the bottom-gate voltage, the contact resistance varies slightly for different electric fields and charge carrier densities.

Apart from a bottom-gate and magnetic-field dependence, the contact resistance of graphite contacts can also depend on temperature. To exclude distortion of our temperature-dependent measurements at high electric fields, we further investigated the resistance as a function of temperature without electric field where the temperature dependence in bilayer graphene is well known. Consistent with previous results[37], we find that the measured resistance only slightly increases with increasing temperature (approximately 750 Ω from 10 mK to 10 K), whereas we see much larger changes in resistance in all the correlated phases in the same temperature range (Extended Data Fig. 10). Thus, we do not expect large changes in our contact resistance with varying temperature.

In Fig. 1a and in the temperature-dependent measurements shown in Fig. 4 and Extended Data Figs. 10 and 12c, we show the measured conductance or resistance (that includes contact resistance) to provide the readers with the original values.

Model Hamiltonian

The following four-band Hamiltonian[23] was used to describe the non-interacting physics near the valley K of BLG

$$H = \begin{bmatrix} \Delta/2 & v_0\pi^\dagger & 0 & v_3\pi \\ v_0\pi & \Delta/2 & \gamma_1 & 0 \\ 0 & \gamma_1 & -\Delta/2 & v_0\pi^\dagger \\ v_3\pi^\dagger & 0 & v_0\pi & -\Delta/2 \end{bmatrix}$$

in the sublattice basis (A_1, B_1, A_2, B_2). Here Δ is the interlayer potential difference, $\pi = p_x + \mathrm{i}p_y$ is the complex momentum operator with p_x and p_y the x and y components of the momentum vector, $a = 0.246$ nm is the graphene lattice constant, $v_i = \frac{\sqrt{3}}{2}\frac{a\gamma_i}{\hbar}$ with $\hbar$ the reduced Planck's constant, and γ_i ($i = 0, 1, 3$) depict the nearest-neighbour intralayer

hopping and the vertical and skew interlayer hopping processes. Other remote hopping processes in the Slonczewski–Weiss–McClure parametrization can be added into the model conveniently but have little effect on any of the calculated results and were thus ignored for simplicity. In the calculations, $\gamma_1 = 400$ meV and $v_3 = 0.1v_0$ were used.

When a perpendicular magnetic field is applied, the momentum operator $\mathbf{p}$ becomes $\mathbf{p} = -i\hbar\nabla + e\mathbf{A}$, where e is the charge of a bare electron, and $\mathbf{A} = (0, Bx)$ is the magnetic vector potential in the Landau gauge. $\pi^\dagger$ and π act as raising and lowering operators of the LLs of a simple quadratic band, that is, $|n\rangle$ ($n = 0, 1, 2...$) with the following identities

$$\pi^\dagger|n\rangle = \frac{i\hbar}{\ell_B}\sqrt{2(n+1)}\,|n+1\rangle,\ \pi|n\rangle = -\frac{i\hbar}{\ell_B}\sqrt{2n}\,|n-1\rangle,\ \pi|0\rangle = 0,$$

where ℓ_B is the magnetic length. To obtain the LLs of trigonally warped BLG, the following eigenstates

$$\left(\sum_n A_n\,|n\rangle,\ \sum_n B_n\,|n\rangle,\ \sum_n C_n\,|n\rangle,\ \sum_n D_n\,|n\rangle\right)^T$$

with a cut-off $N_c = 100$ were constructed to diagonalize the Hamiltonian. Diagonalizing the coefficient matrix in the basis (A_0, B_0, C_0, D_0, A_1, B_1, C_1, D_1, ...) produced the LL structure in Fig. 1d.

Generalized Wigner–Seitz radius

To evaluate the important roles of electron–electron interactions in a low-density electron gas system, it is suggested to examine the dimensionless Wigner–Seitz radius[27] $r_s = U/W$, where $U = e^2\sqrt{\pi n}/\epsilon$ is the estimated Coulomb potential, W is the average kinetic (band) energy of electrons/holes with respect to the band bottom/top, n is the charge carrier density and ϵ is the dielectric constant. The r_s calculation is extremely neat for a perfect quadratic band with a constant isotropic effective mass, and W turns out to be exactly half of the Fermi energy E_F in two dimensions. However, the r_s calculation is complex for the current case, because the Fermi surface is trigonally warped, because the effective mass varies strongly with momentum and electric field, and because the electron and hole pockets can coexist in between the two Lifshitz transitions. Nevertheless, the net charge density n and the average kinetic energy W were naturally defined as follows

$$n = \int_{E>E_F} \frac{d^2\mathbf{k}}{(2\pi)^2},\ W = \frac{1}{n}\int_{E>E_F} [E_M - E_\mathbf{k}]\frac{d^2\mathbf{k}}{(2\pi)^2},$$

where $E_\mathbf{k}$ is the band energy at momentum $\mathbf{k}$, and E_M is the valence-band energy maximum. When the electron and hole pockets coexist, the charge density n_e, the average kinetic energy W_e and the estimated Coulomb potential U_e for the electrons in the inner (in) pocket were naturally defined as follows

$$n_e = \int_{E<E_F,\,\mathbf{k}\in in} \frac{d^2\mathbf{k}}{(2\pi)^2},\ W_e = \frac{1}{n_e}\int_{E<E_F,\,\mathbf{k}\in in} [E_\mathbf{k} - E_0]\frac{d^2\mathbf{k}}{(2\pi)^2},\ U_e = \frac{e^2\sqrt{\pi n_e}}{\epsilon},$$

where $E_\mathbf{0}$ is the band energy at $\mathbf{k} = 0$. It follows that the charge density n_h, the average kinetic energy W_h and the estimated Coulomb potential U_h for the holes in the outer pocket(s) read

$$n_h = n + n_e,\ W_h = W + W_e,\ U_h = \frac{e^2\sqrt{\pi n_h}}{\epsilon}.$$

Thus, for the electrons $r_s = U_e/W_e$, whereas for the holes $r_s = U_h/W_h$. When the inner electron pocket is absent, $r_s = U_h/W_h = U/W$. In the estimations, the experimentally extracted $\epsilon = 3$ was used.

Calculations of LLs and r_s values

In Fig. 1, the experimental fan diagram at $E = 0.6$ V nm^{-1} and two types of theoretical calculation are compared. First, by using experimental relevant parameter values, we can estimate the interlayer potential difference Δ to be around $0.25\gamma_1$, and then calculate the LL structure for the non-degenerate valence band. The LL crossings between the $\nu = -4$ and $\nu = -5$ QH states are well matched between the experiment (Fig. 1c) and the calculation (Fig. 1d). Next, we use the same set of parameters to calculate the Wigner–Seitz radius r_s as a function of the charge carrier density n.

First, assuming a four-fold (spin and valley) degeneracy for all the states, we find that no Lifshitz transition can be reached in the density range of the experimental fan diagram, and that the corresponding r_s (black curve in Fig. 1e) is always larger than 34, a threshold for the Wigner crystallization of 2D electron gases[27], not to mention 20, a threshold for the ferromagnetic instability of 2D electron gases[27]. Following this result, next, we assume all the states to be ferromagnetic and two-fold (either spin or valley) degenerate, and find that both Lifshitz transitions can be reached, and that the r_s values (red curves in Fig. 1e) of the outer hole (h^+) and inner electron (e^-) pockets are generally larger than 20. Following this result, lastly, we assume all the ferromagnetic states to be non-degenerate, and find that both Lifshitz transitions can be reached, and that the r_s (blue curves in Fig. 1e) of the outer hole (inner electron) pocket is smaller (larger) than 20 (34).

Relation between critical densities and correlated phases

When compared with our experimental findings, these theoretical calculations at least suggest the following five facts. (1) The observed LL crossing can be attributed to the annular Fermi surface in between the two Lifshitz transitions of the quarter metal (Fig. 1d). Consistently, a similar crossing can be seen at $B = 2.4$ T and $n = -4 \times 10^{11}$ cm^{-2} (Fig. 1c), near which the half metal has an annular Fermi surface. (2) The result $r_s < 20$ for the non-degenerate case is consistent with that phase A is a non-degenerate quarter metal at low densities where there is no inner electron pocket. (3) The result $r_s > 34$ for the non-degenerate electron pocket is consistent with that phases II and III are non-degenerate Wigner crystals. In addition, we observe indications of another insulating phase similar to phase II (phase V, only at finite B; Extended Data Fig. 12) near the density in which the doubly degenerate inner electron pocket is present, consistent with the result $r_s > 34$ for the doubly degenerate electron pocket. (4) Phases I and IV are metallic, with very similar behaviour in temperature (Fig. 4), bias current (Fig. 3f), and both in-plane and out-of-plane magnetic fields (Extended Data Figs. 6 and 7). This is consistent with that they both occur in a density range close to but below the Lifshitz transition associated with the vHS. (5) The phase boundary between D and C and that between C and B at $E = 0.6$ V nm^{-1} (Fig. 2c) are almost coincident with the two calculated Lifshitz transition densities for the states being doubly degenerate (half metal), that is, the boundaries of the light red shaded region in Fig. 1e.

Diophantine equation and Wigner–Hall crystals

Wigner–Hall physics can be captured by the Diophantine equation $n = \nu n_\phi + \eta A_0^{-1}$, where ν is the total Chern number, $n_\phi = eBh^{-1}$ is the density of magnetic flux quanta, η is the band filling and A_0 is the unit cell area of electron crystal[17]. A Wigner crystal has $\nu = 0$ and $\eta \neq 0$ (for example, phase III), whereas a Hall crystal or a QH state has $\nu \neq 0$ and $\eta = 0$. The more unusual case for $\nu \neq 0$ and $\eta \neq 0$ is the Wigner–Hall crystal. For phase II, one possible scenario is $\nu = -2$ and $\eta \neq 0$: the doped holes spontaneously crystallize with the formation of Chern bands[7,38], or they form a Wigner crystal on top of the undoped system that is in one state of the QAH octet[7,13].

Device quality

Extended Data Fig. 3a shows the conductance plotted as a function of the density and the magnetic field at $E = 0.0$ V nm^{-1}. It is clear that the lowest QH states start to emerge at very low magnetic fields of 0.2 T, demonstrating the high quality of our device[13]. At higher magnetic fields, all integer filling factors appear owing to spontaneous symmetry breaking[6]. Extended Data Fig. 3c shows the conductance as a function of the density and the electric field at $B = 2$ T. All integer QH states are clearly visible. In addition, one can see several transitions in the electric field that mark the collapse of different LLs owing to the interplay of spin and valley splitting[34]. We further investigated the $\nu = 0$ QH state as a function of the electric field and the magnetic field (Extended Data Fig. 3d). We observed unusual sharp conductance peaks marking the transition between the canted antiferromagnetic phase and the fully layer polarized phase. This underlines the high quality of our device[39].

The conductance map shows slight asymmetry in electric field, probably owing to the different cleanliness levels of the two sides of BLG. Nevertheless, the main signatures described are the same for both the negative and positive electric fields.

Additional magnetotransport data

In the main text, we have focused on the hole side where the most distinct features were observed. Although we did not find signatures of phases I–IV on the electron side (Fig. 1a), there could be Stoner phases in the conduction band. In Extended Data Fig. 2, we show the derivative of the conductance as a function of the filling factor ν ($\nu > 0$) and the electric field and highlight regions with two-fold and four-fold degeneracies that potentially correspond to half and full metal phases. For completeness, the conductance as well as its derivative as functions of the charge carrier density and the magnetic field are shown in Extended Data Fig. 6 for different electric fields not shown in the main text. Furthermore, the derivative of the conductance as a function of the charge carrier density and the magnetic field at an electric field of -0.8 V nm^{-1} is shown for a second device (device B) in Extended Data Fig. 4. Even though device B is not as clean as device A, we still identified all the phases discussed in the main text. The four phases I–IV show approximately the same density, electric field and magnetic field behaviour in both devices (Extended Data Fig. 8).

Data availability

The data that support the findings of this study are available from the corresponding authors upon reasonable request.

32. Taniguchi, T. & Watanabe, K. Synthesis of high-purity boron nitride single crystals under high pressure by using Ba–BN solvent. *J. Cryst. Growth* **303**, 525–529 (2007).
33. Winterer, F. et al. Spontaneous gully-polarized quantum Hall states in ABA trilayer graphene. *Nano Lett.* **22**, 3317–3322 (2022).
34. Lee, K. et al. Chemical potential and quantum Hall ferromagnetism in bilayer graphene. *Science* **345**, 58–61 (2014).
35. Li, J., Tupikov, Y., Watanabe, K., Taniguchi, T. & Zhu, J. Effective Landau level diagram of bilayer graphene. *Phys. Rev. Lett.* **120**, 47701 (2018).
36. Freitag, F., Trbovic, J., Weiss, M. & Schönenberger, C. Spontaneously gapped ground state in suspended bilayer graphene. *Phys. Rev. Lett.* **108**, 76602 (2012).
37. Das Sarma, S., Hwang, E. H. & Rossi, E. Theory of carrier transport in bilayer graphene. *Phys. Rev. B* **81**, 161407 (2010).
38. Haldane, F. D. M. Model for a quantum Hall effect without Landau levels: condensed-matter realization of the "parity anomaly". *Phys. Rev. Lett.* **61**, 2015–2018 (1988).
39. Maher, P. et al. Evidence for a spin phase transition at charge neutrality in bilayer graphene. *Nat. Phys.* **9**, 154–158 (2013).

Acknowledgements We thank V. I. Fal'ko, L. Levitov, A. H. MacDonald and Di Xiao for discussions. R.T.W. and A.M.S. acknowledge funding from the Center for Nanoscience (CeNS) and by the Deutsche Forschungsgemeinschaft (DFG, German Research Foundation) under the SFB 1073 project B10 and under Germany's Excellence Strategy-EXC-2111-390814868 (MCQST). T.X. and F.Z. acknowledge support from the Army Research Office under grant number W911NF-18-1-0416 and the National Science Foundation under grant numbers DMR-1945351 through the CAREER programme, DMR-2105139 through the CMP programme, and DMR-1921581 through the DMREF programme. K.W. and T.T. acknowledge support from the Elemental Strategy Initiative conducted by the MEXT, Japan (grant number JPMXP0112101001) and JSPS KAKENHI (grant numbers 19H05790, 20H00354 and 21H05233).

Author contributions A.M.S. fabricated the devices and conducted the measurements and data analysis. K.W. and T.T. grew the hexagonal nitride crystals. T.X. performed the calculations and contributed to the theories. F.Z. supervised the computational and theoretical parts. All authors discussed and interpreted the data. R.T.W. supervised the experiments and the analysis. The manuscript was prepared by A.M.S., F.Z. and R.T.W. with input from all authors.

Competing interests The authors declare no competing interests.

Additional information

Supplementary information The online version contains supplementary material available at https://doi.org/10.1038/s41586-022-04937-1.

Correspondence and requests for materials should be addressed to Fan Zhang or R. Thomas Weitz.

Peer review information *Nature* thanks Dong-Keun Ki, Folkert de Vries and the other, anonymous, reviewer(s) for their contribution to the peer review of this work. Peer reviewer reports are available.

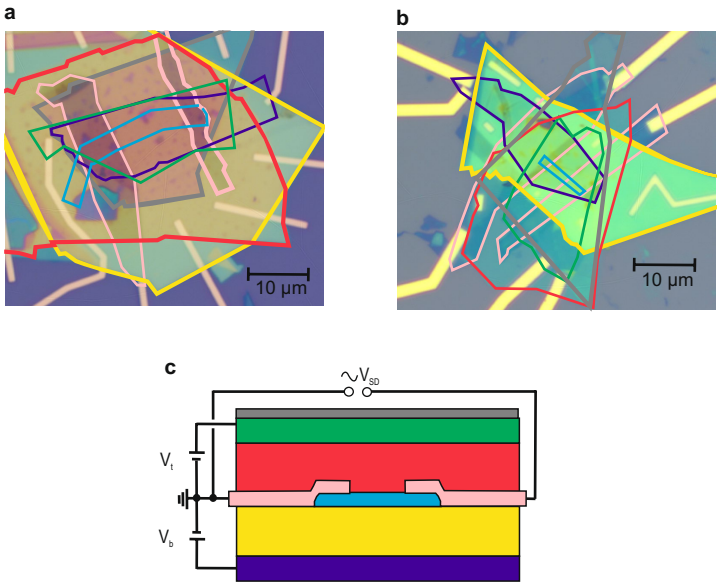

Extended Data Fig. 1 | Bilayer graphene devices studied here. a, **b**, Optical images of device A (presented in the main manuscript) (**a**) and device B (**b**). The top hBN is encircled in grey, the upper graphite flake in green, the upper hBN flake in red, the graphite contacts in pink, the bilayer graphene flake in blue, the lower hBN flake in yellow, and the lower graphite flake in purple. **c**, Schematic of the bilayer graphene devices. The colours of different flakes match those in **a**, **b**.

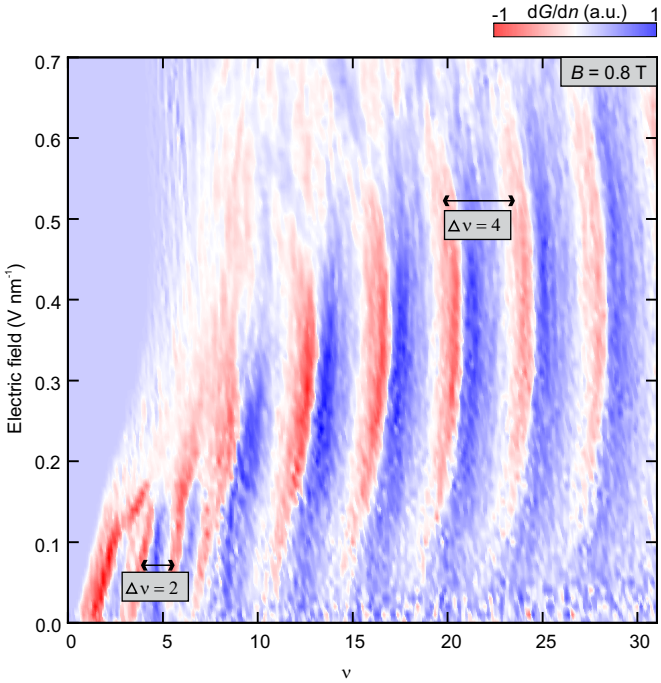

Extended Data Fig. 2 | Stoner physics in the conduction band. Density derivative of the conductance as a function of the filling factor ν and the electric field at $B = 0.8$ T for positive filling factors. Two-fold and four-fold LL degeneracies are marked.

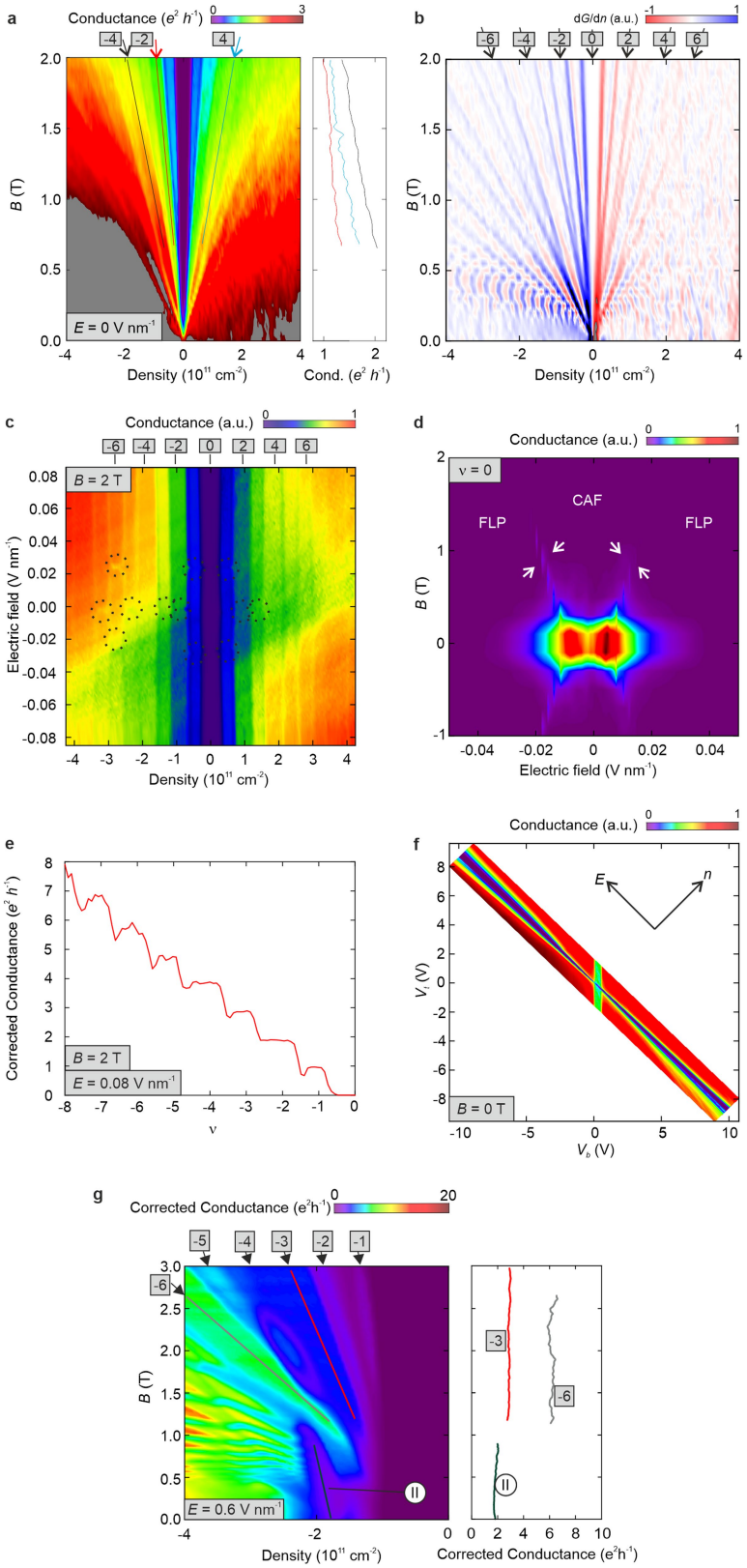

Extended Data Fig. 3 | See next page for caption.

Extended Data Fig. 3 | Device Characterizations. a, Fan diagram at $E = 0$ V/nm. The QH states $\nu = -4, -2$, and 2 are traced as function of the magnetic field and the charge carrier density. **b**, Derivative of the conductance in **a**. **c**, Conductance as a function of the charge carrier density and the electric field at $B = 2$ T. Transitions induced by the electric field are marked by dashed circles. (In **a**–**c**, Integer QH states are labelled by numerals.) **d**, Conductance as a function of the electric field and the magnetic field at $\nu = 0$. The phase transitions between the canted antiferromagnetic (CAF) and fully layer polarized (FLP) phases are indicated by arrows. **e**, Conductance as a function of the charge carrier density at $E = 0.08$ V/nm and $B = 2$ T (extracted from data in **c**). Here a contact resistance of 7800 Ω was subtracted. **f**, Conductance as a function of the top and bottom-gate voltages at $B = 0$ T in the space of -7×10^{11} cm$^{-2} < n < 7 \times 10^{11}$ cm^{-2} and -0.7 V/nm $< E < 0.7$ V/nm. **g**, Conductance as a function of charge carrier density and magnetic field at $E = 0.6$ V/nm. A contact resistance of $R_c = 2000\,\Omega + 3000\,\Omega/\mathrm{T} \times B\,(\mathrm{T})$ was subtracted from the measured values. The data are the same measurements presented in Fig 1c of the main manuscript.

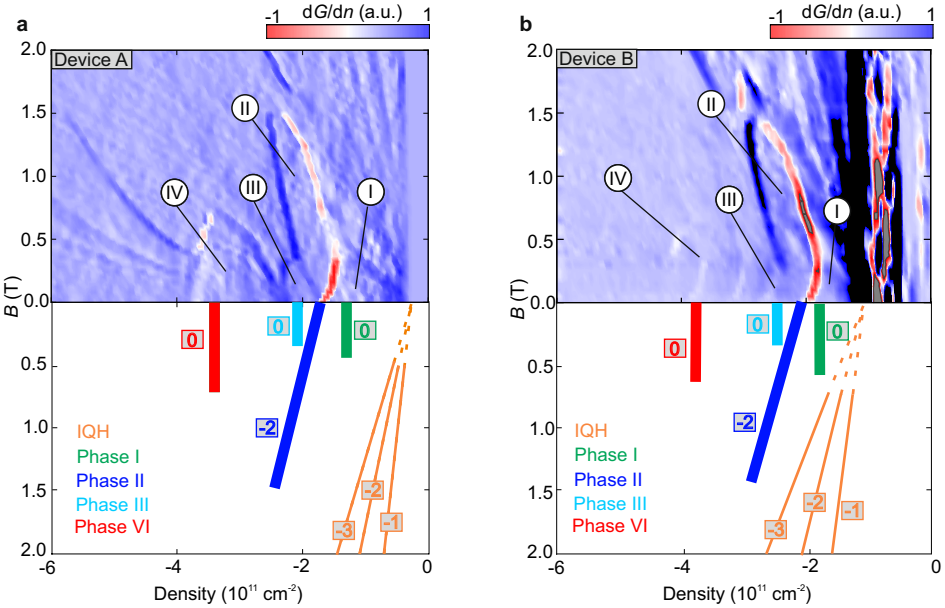

Extended Data Fig. 4 | Magnetotransport data of a second device. Density derivative of the conductance plotted as a function of the charge carrier density and the magnetic field at $E = -0.8$ V/nm for device A (shown in the main manuscript) (**a**) and device B (**b**). The slopes of the lowest integer QH states and of the phases I–IV discussed in the main text are traced by lines in the mirror schematics of the fan diagrams. The corresponding slopes are indicated by arabic numerals. The lines are solid if the states are present and dashed otherwise.

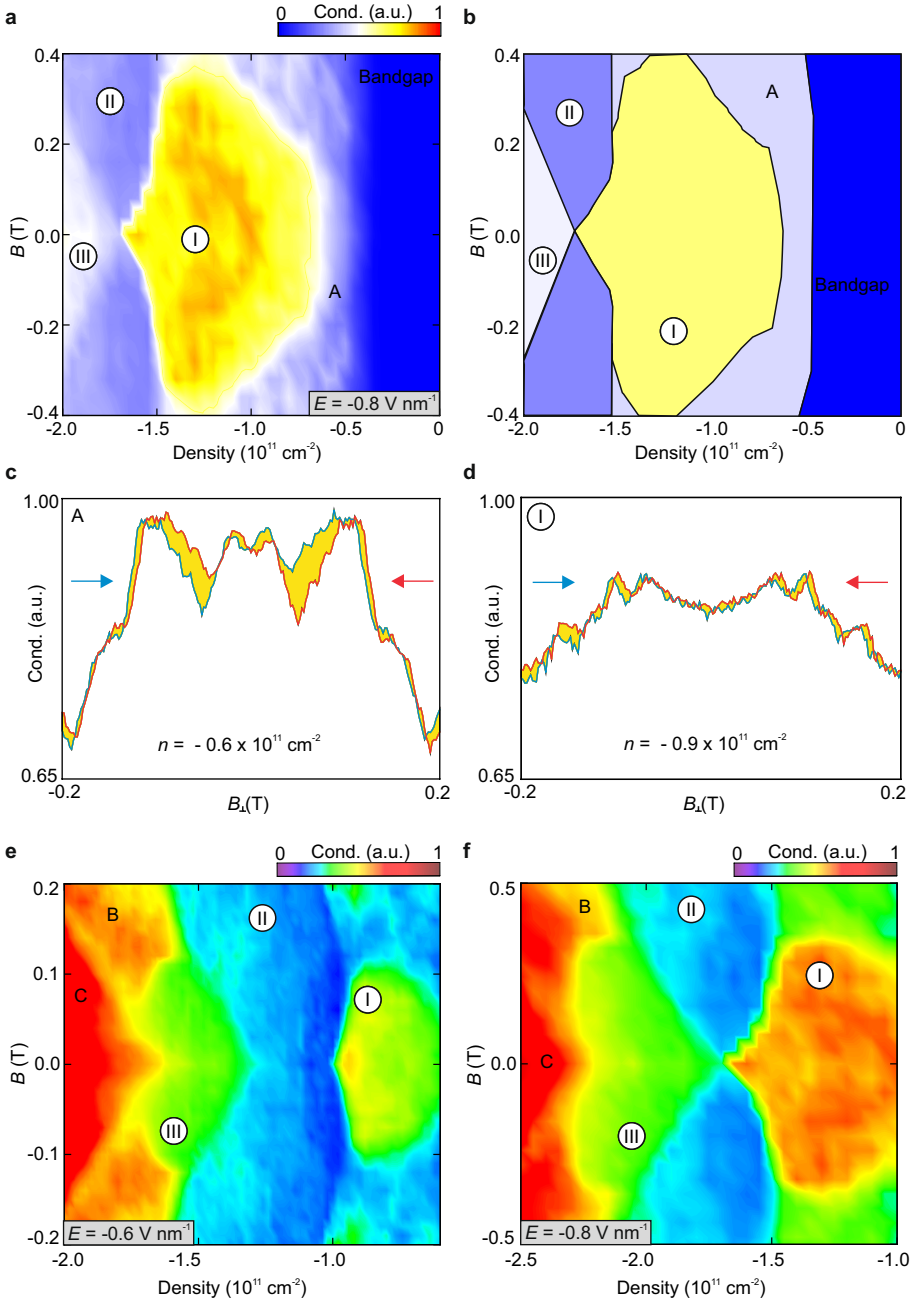

Extended Data Fig. 5 | Zoom-in of phases I–III and A. a, Conductance as a function of charge carrier density and magnetic field at $E = -0.8$ V/nm showing the clear distinction between phases I and A. **b**, Schematic of phases A and I-III at $E = -0.8$ V/nm. **c,d**, Magnetic hysteresis of phase A (**c**)and phase I (**d**). The forward sweeps are shown in blue while the backward ones in red. The hysteresis loop areas are shaded in yellow. **e**, **f**, Conductance as a function of charge carrier density and magnetic field at $E = -0.6$ V/nm (**e**) and $E = -0.8$ V/nm (**f**) showing the clear distinction between phases I, II and III and B and C that show distinct values in conductance and clear steps of conductance at the phase boundaries.

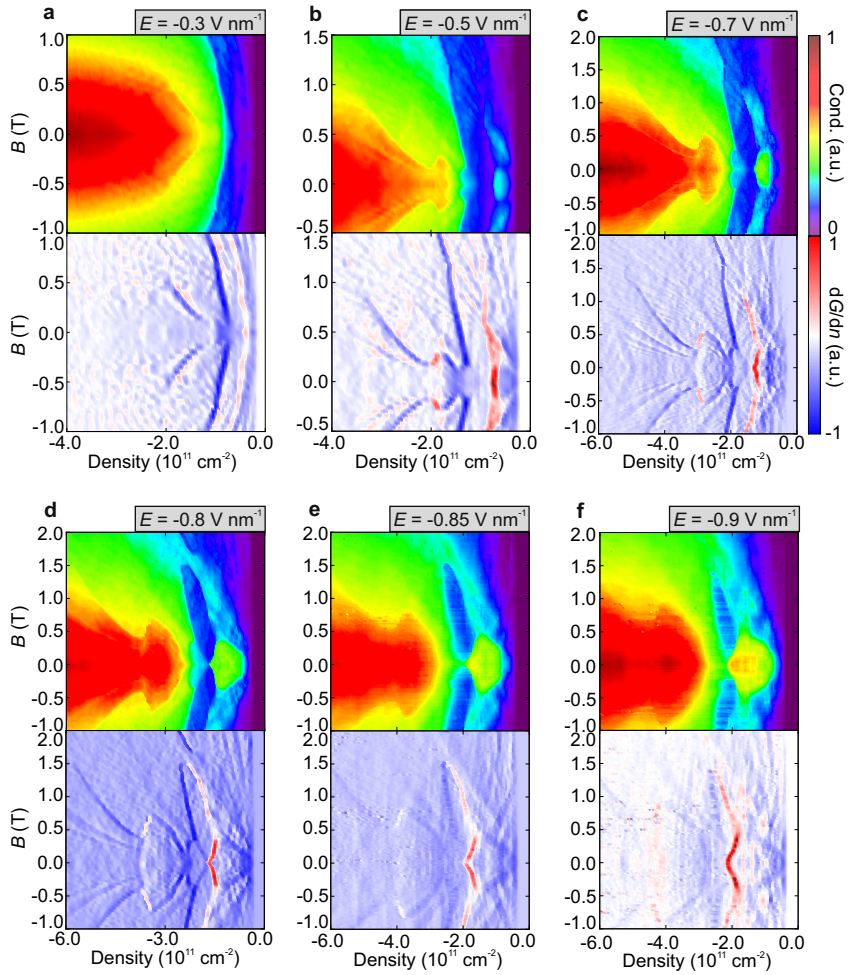

Extended Data Fig. 6 | Additional magnetotransport data at various electric fields. Conductance and its density derivative plotted as functions of the charge carrier density and the magnetic field at different electric fields.

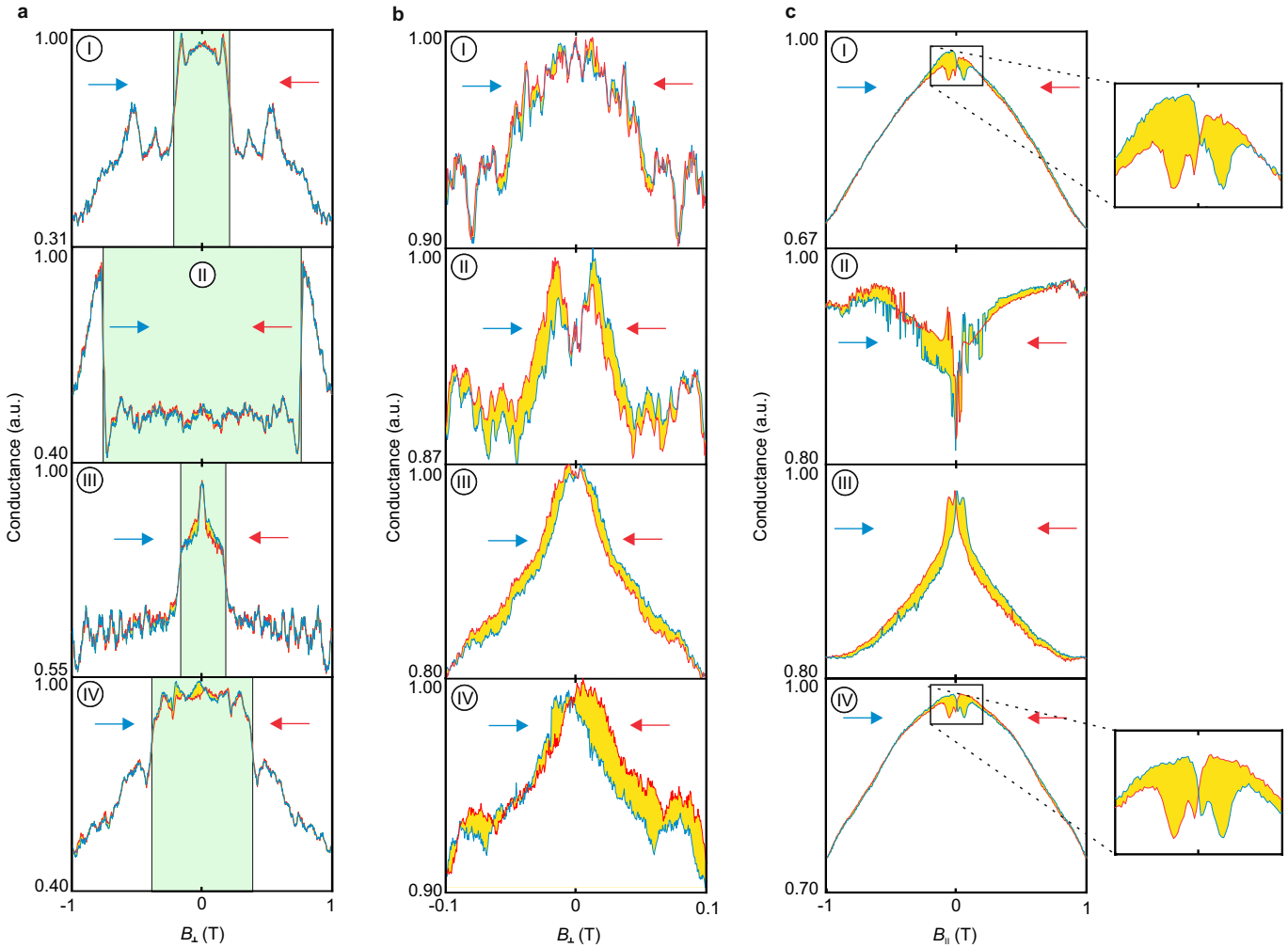

Extended Data Fig. 7 | Magnetic field hysteresis of phases I–IV. Hysteresis of the conductance as a function of the out-of-plane magnetic field $B_\perp$ (**a**, **b**) and the in-plane magnetic field $B_\parallel$ (**c**) at $E = -0.6$ V/nm and charge carrier densities corresponding to phase I ($n = -0.85 \times 10^{11}$ cm^{-2}), phase II ($n = -1.2 \times 10^{11}$ cm^{-2}), phase III ($n = -1.5 \times 10^{11}$ cm^{-2}), and phase IV ($n = -2.2 \times 10^{11}$ cm^{-2}), respectively. The forward sweeps are shown in blue while the backward ones in red. The hysteresis loop areas are shaded in yellow. The data shown in **a**, **b** stem from two different sets of measurement. The magnetic field sweeps were started at −1 T and −0.1 T respectively. In (a) the $B_\perp$ ranges in which phases I–IV are stable are highlighted in green.

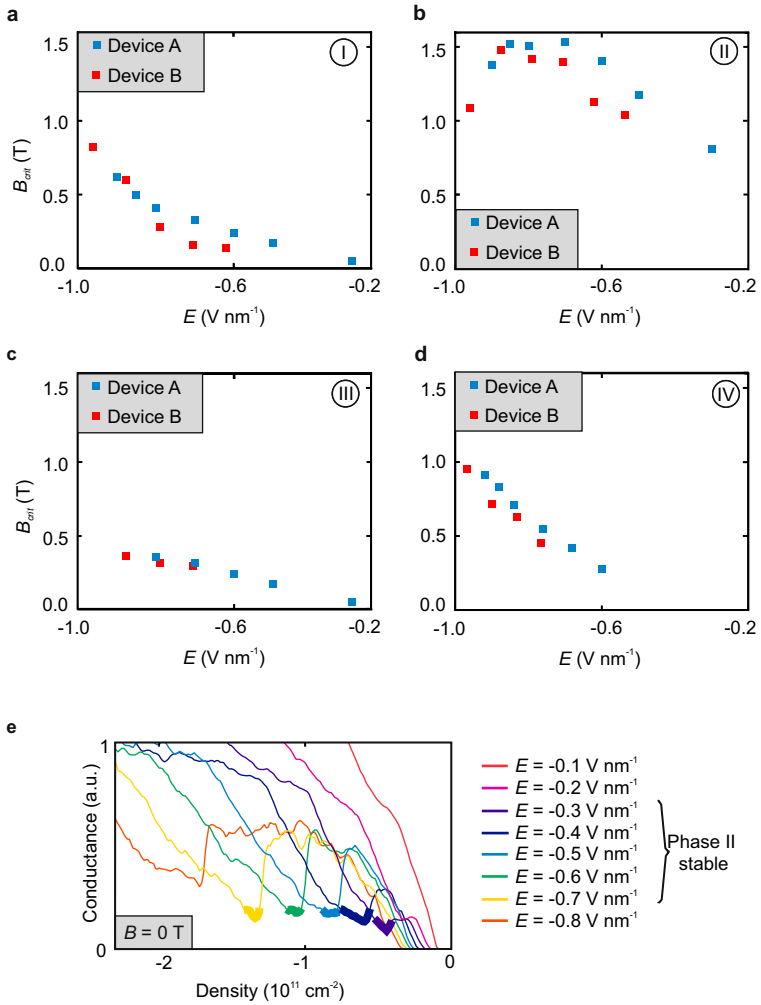

Extended Data Fig. 8 | Critical magnetic fields and conductance of phase II at various different electric fields. a–**d**, Critical magnetic fields for devices A and B of phase I (**a**), phase II (**b**), phase III (**c**), and phase IV (**d**) at different electric fields. **e**, Conductance as a function of charge carrier density at different electric fields and $B = 0$. Density regions of stable phase II are highlighted.

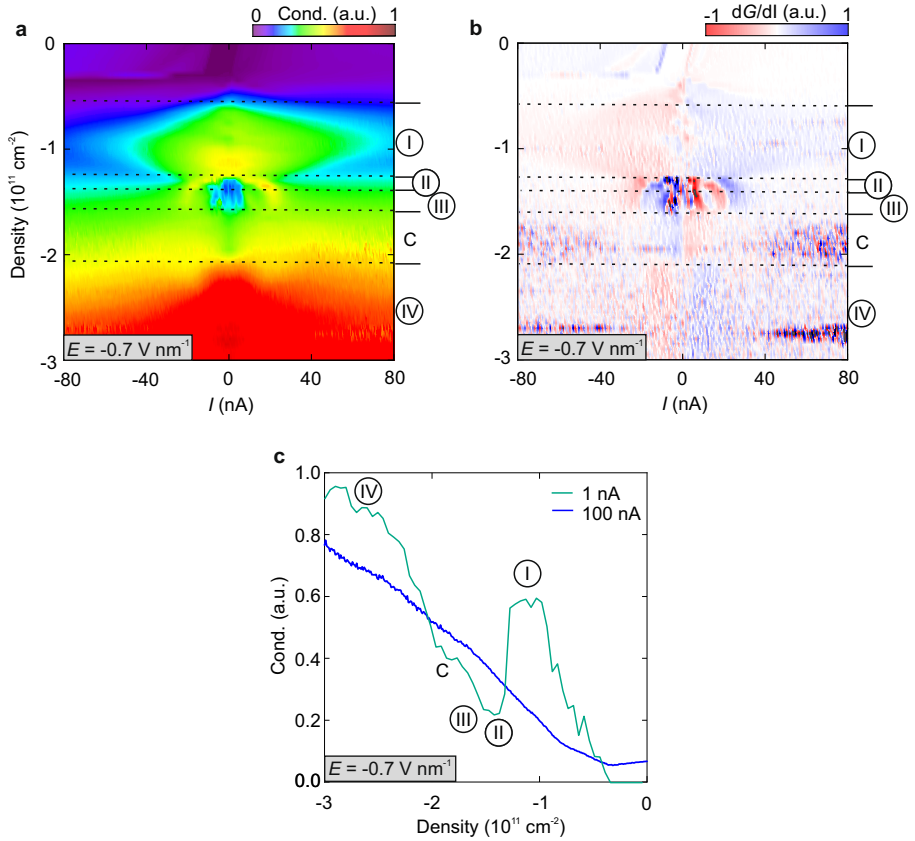

Extended Data Fig. 9 | Current dependent measurements. a, **b**, Conductance (**a**) and bias current derivative of conductance (**b**) as a function of bias current I and charge carrier density n at $E = -0.7$ V/nm and $B = 0$ showing a gap in phases II and III at small currents. **c**, Conductance as a function of n at $E = -0.7$ V/nm and $B = 0$ for $I = 100$ nA (blue) and $I = 1$ nA (green). The phases I – IV can not be seen at large currents, indicative of the many-body nature of the phases.

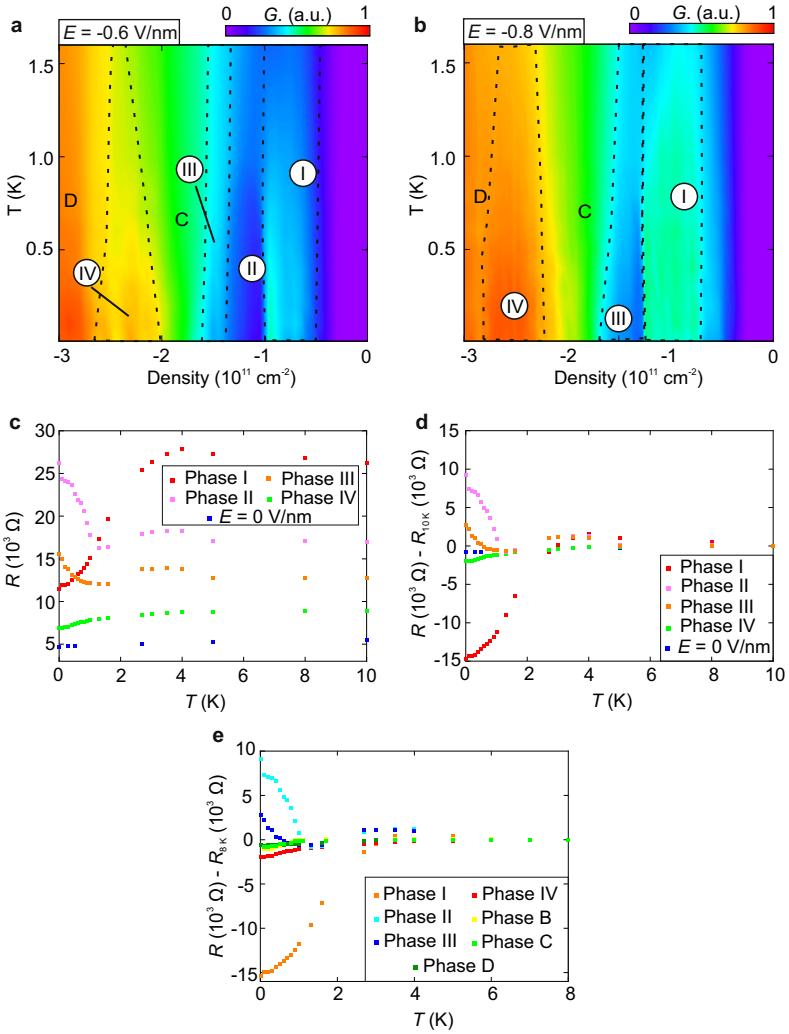

Extended Data Fig. 10 | Temperature dependence of phases I–IV and B–D. **a**, **b**, Conductance as a function of charge carrier density and temperature T at $B = 0$ and $E = -0.6$ V/nm (**a**) and $B = 0$ and $E = -0.8$ V/nm (**b**).**c**, **d**, R(**c**) and $R - R$ (10K) (**d**) as a function of temperature T for phase I ($n = -0.9 \times 10^{11}$ cm^{-2}), phase II ($n = -1.2 \times 10^{11}$ cm^{-2}), phase III ($n = -1.5 \times 10^{11}$ cm^{-2}), and phase IV ($n = -2.2 \times 10^{11}$ cm^{-2}) at $E = 0.6$ V/nm and for the normal state at $E = 0$ V/nm ($n = -1.0 \times 10^{11}$ cm^{-2}). **e**, $R - R$ (8K) as a function of temperature T for phase I ($n = -0.9 \times 10^{11}$ cm^{-2}), phase II ($n = -1.2 \times 10^{11}$ cm^{-2}), phase III ($n = -1.5 \times 10^{11}$ cm^{-2}), and phase IV ($n = -2.2 \times 10^{11}$ cm^{-2}) at $E = -0.6$ V/nm and $B = 0$ T and for the phase B ($n = -2.2 \times 10^{11}$ cm^{-2}), phase C ($n = -2.5 \times 10^{11}$ cm^{-2}), and phase D ($n = -4.0 \times 10^{11}$ cm^{-2}) at $E = -0.6$ V/nm and $B = 0.6$ T.

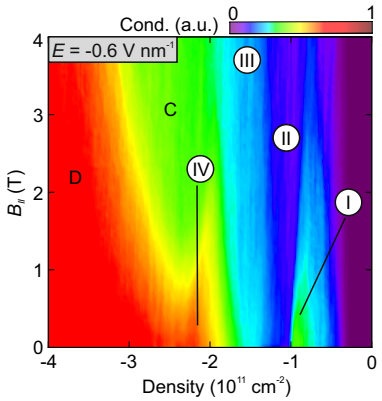

Extended Data Fig. 11 | In-plane magnetic field dependence of phases I–IV. Conductance as a function of charge carrier density and in-plane magnetic field $B_{||}$ at $B_{\perp} = 0$ and $E = -0.6$ V/nm. The phase boundary between phase II and III does not shift with increasing the in-plane magnetic field suggesting that both phases likely carry similar in-plane spin order and inter-valley coherence. Compared with phase I, both phases likely have larger magnitudes of spin polarization since they are more stable against large in-plane magnetic fields.

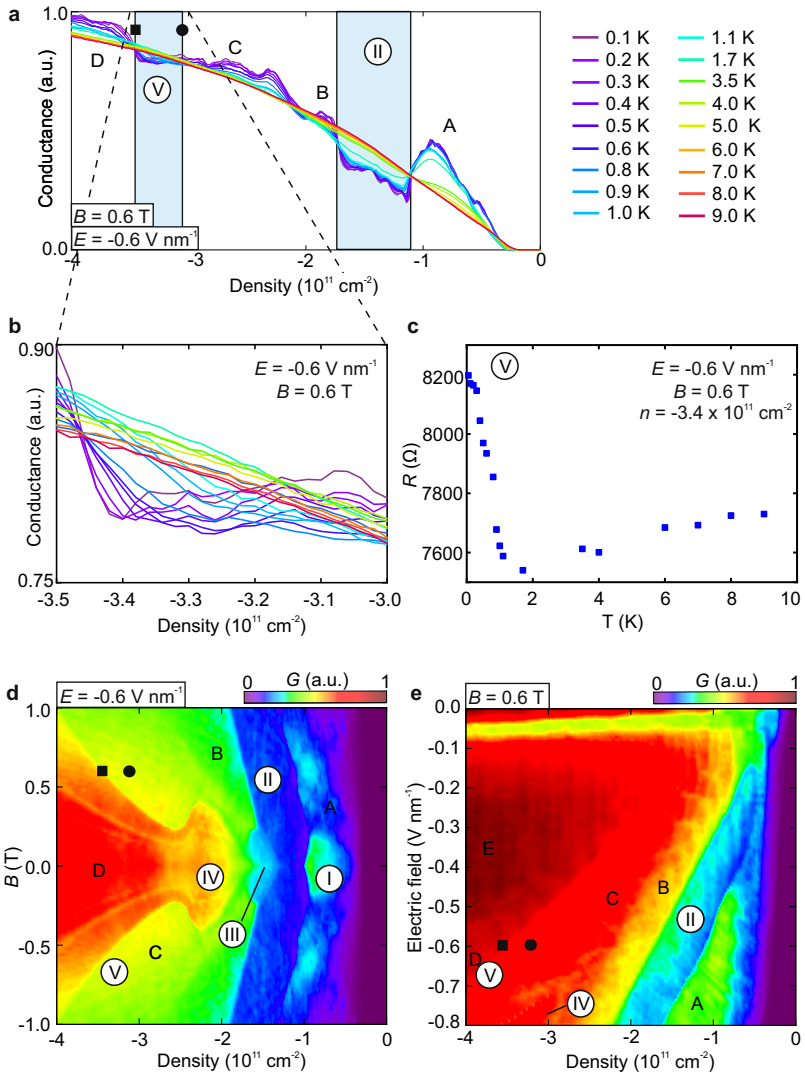

Extended Data Fig. 12 | Experimental indications of a further novel phase close to the Lifshitz transition of the half metal, termed phase V. We find this additional phase near the density in which the doubly degenerate inner electron pocket is present, consistent with the result $r_s > 34$ (dashed red) for the electron pocket in Fig 1e of the main manuscript. Potentially this phase resembles phase II and/or III but for the doubly degenerate case. **a**, Conductance as a function of charge carrier density for different temperatures at $E = -0.6$ V/nm and $B = 0.6$ T. The insulating correlated phases are highlighted in blue. The maximum/minimum charge carrier density at which phase V is stable is marked by a black square/circle. **b**, Zoom-in of **a** around phase V. **c**, Resistance as a function of temperature T for phase V at $E = -0.6$ V/nm, $B = 0.6$ T, and $n = -3.4 \times 10^{11}$ cm^{-2}. **d**, Conductance as a function of charge carrier density and magnetic field at $E = -0.6$ V/nm. The maximum/minimum charge carrier density at which phase V is stable at $B = 0.6$ T is marked by a black square/circle. **e**, Conductance as a function of charge carrier density and electric field at $B = 0.6$ T. The maximum/minimum charge carrier density at which phase V is stable at $E = -0.6$ V/nm is marked by a black square/circle.